Article

Location-aware ingestible microdevices for wireless monitoring of gastrointestinal dynamics

In the format provided by the authors and unedited
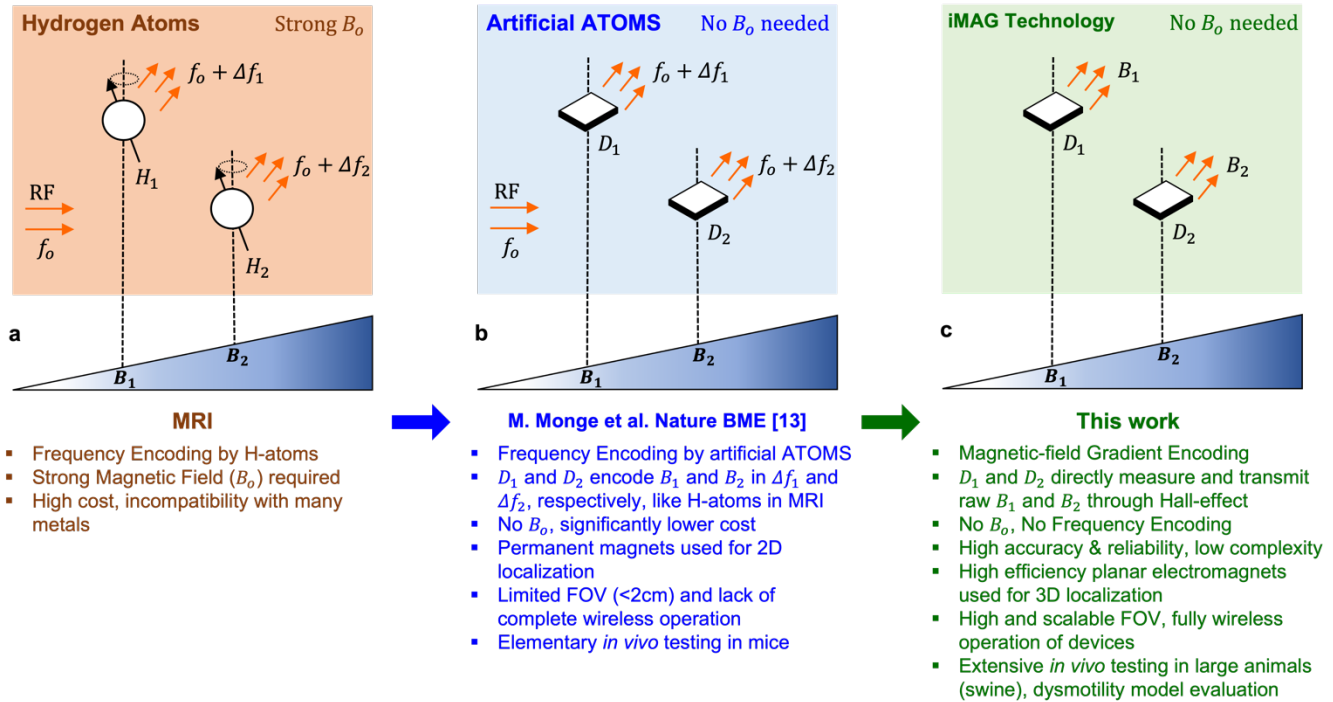
Fig. 1: (a) Frequency encoding performed in MRI using hydrogen atoms. **(b)** Micro-chips working as artificial atoms to perform frequency encoding without any B_0 [13]. **(c)** Micro-chips localized using magnetic-field gradient encoding, eliminating both B_0 and frequency encoding in this work.
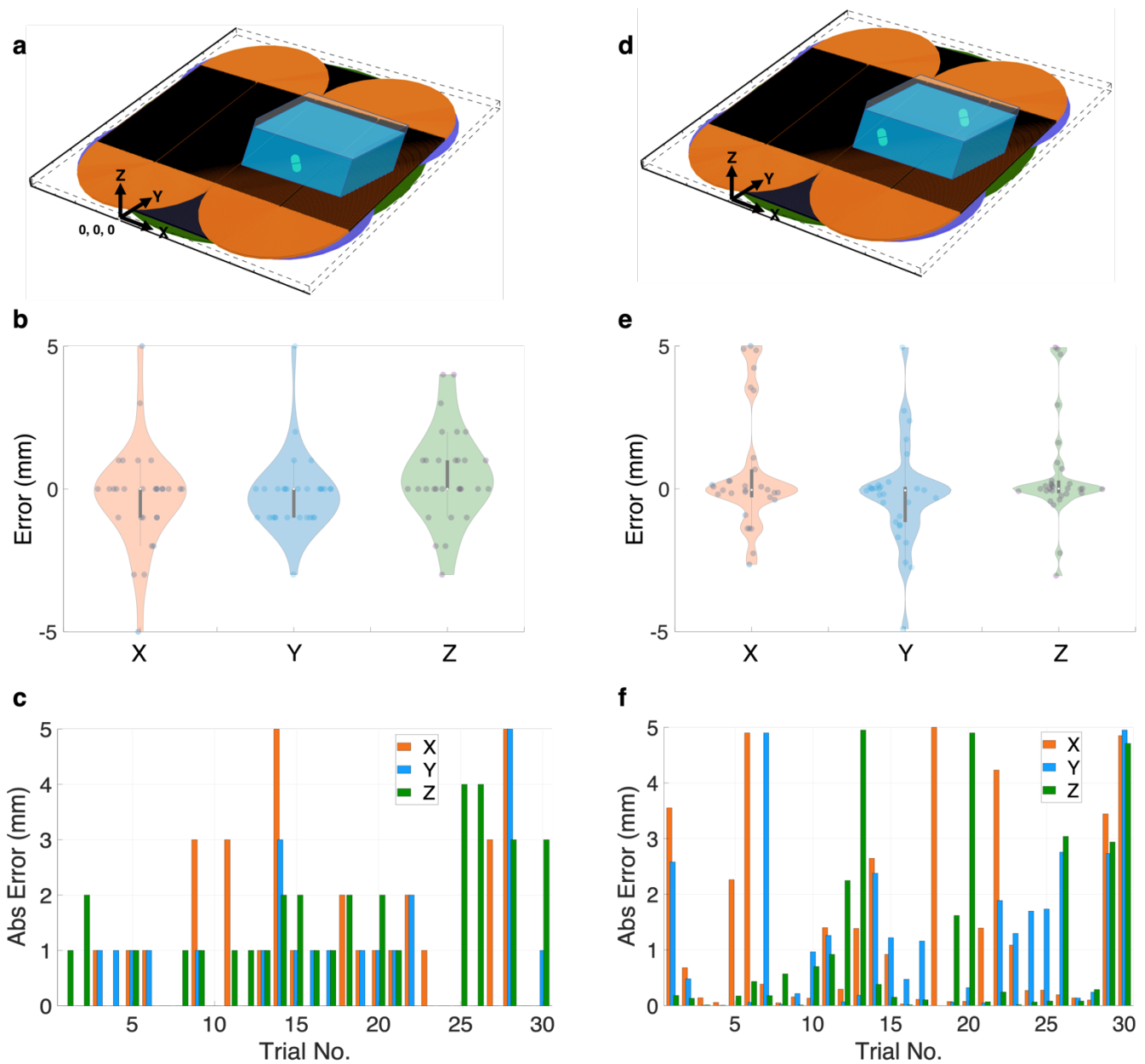
Fig. 2: (a) *In vitro* localization of a single iMAG with respect to the global origin (0,0,0) of the coils at n=30 different locations chosen uniformly in the FOV. **(b)** Errors at all 30 locations clustered together. **(c)** Error at each location is plotted separately. Reported as mean $\pm$ std: 1.07 ± 1.44mm (X), 0.77 ± 1.07mm (Y), 1.13 ± 1.20mm (Z). **(d)** *In vitro* localization of iMAG with respect to another iMAG at a known location serving as a relative reference. This eliminates the need for a global reference point. n=30 different locations were chosen uniformly in the FOV. **(e), (f)** Error in the decoded position of iMAG localized with respect to a reference iMAG. Error as mean $\pm$ std: 1.34 ± 1.68mm (X), 1.13 ± 1.38mm (Y), 0.97 ± 1.55mm (Z).
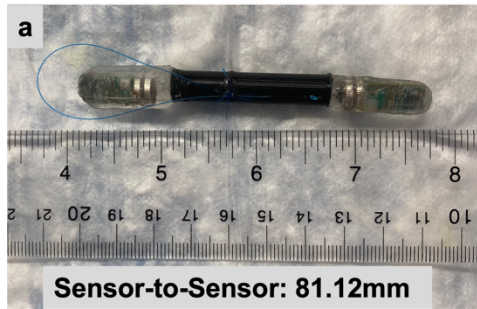
b *In vivo* Measurement Data

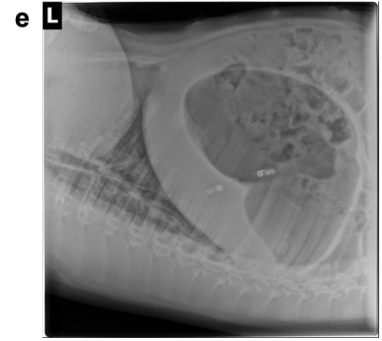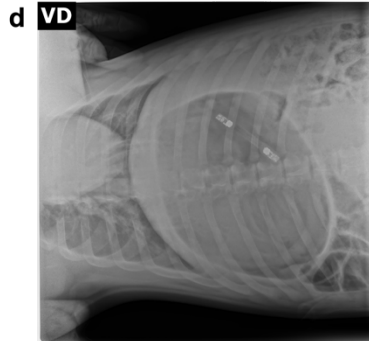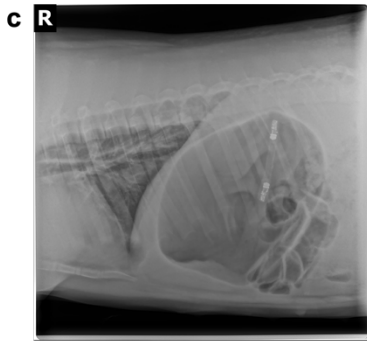| Trial	Decoded Distance (mm)	|X-Error| (mm)	|Y-Error| (mm)	|Z-Error| (mm)
1	84.3630	2.7032	1.6418	0.7165
2	82.9760	1.5728	0.8359	0.5211
3	83.4571	1.9692	1.1960	0.3915
Mean	83.5987 $\pm$ 0.7043	2.0817	1.2246	0.5430

Sensor-to-Sensor: 81.12mm

Fig. 3: (a) A test fixture was prepared with two iMAG devices positioned a fixed distance apart (81.12mm) and lodged into the gastric cavity of the pig via an endoscope. **(b)** *In vivo* measurement data for three consecutive trials while the fixture is inside the gastric cavity of the pig. The decoded inter-device distance from iMAG is 83.6 ± 0.7 mm (mean $\pm$ std). Individual errors in the X, Y and Z components of the decoded distance are <5mm, the theoretical error-bound of our system. **(c)** Right, **(d)** vertical, and **(e)** left sided X-ray scans of the animal showing the position of the fixture.

iMAG in Stomach

Ground truth from
X-rays: 24.44cm

In vivo Measurement Data

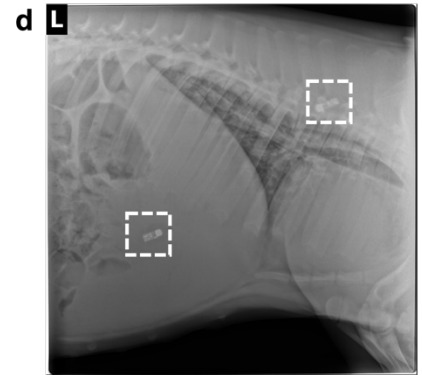| Trial	Decoded Distance (cm)	|X-Error| (mm)	|Y-Error| (mm)	|Z-Error| (mm)
1	24.5540	0.9101	0.4960	0.4763
2	24.5188	0.6458	0.3089	0.3295
3	24.3380	0.8000	0.4252	0.4688
Mean	**24.4703 $\pm$ 0.1159**	**0.7853**	**0.4100**	**0.4249**
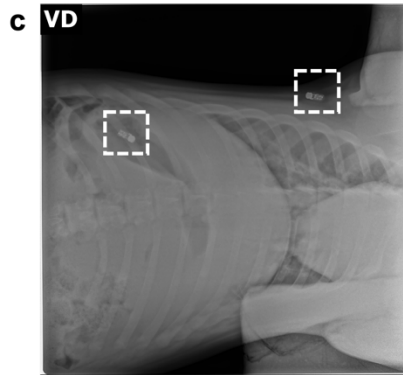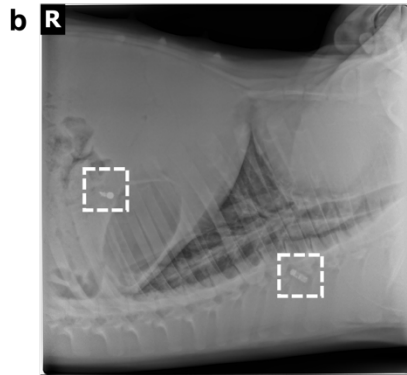
Fig. 4: (a) *In vivo* measurement data when iMAG is located inside the stomach of the pig. The ground truth (24.44cm) is obtained using orthogonal X-rays taken from the (b) right, (c) vertical, and (d) left side of the animal. The decoded distance of iMAG from the external reference iMAG is 24.47 $\pm$ 0.12 cm (mean $\pm$ std). Individual errors in the X, Y and Z components of the decoded distance are <5mm, the theoretical error-bound of our system.

iMAG in Colon

Ground truth from
X-rays: 21.37cm

In vivo Measurement Data

| Trial	Decoded Distance (cm)	|X-Error| (mm)	|Y-Error| (mm)	|Z-Error| (mm)
1	20.2005	7.2703	8.9638	1.8886
2	20.2115	7.3742	8.9790	1.9251
3	20.1985	7.2105	8.9101	1.8210
Mean	20.2035 $\pm$ 0.0070	7.2850	8.9510	1.8782
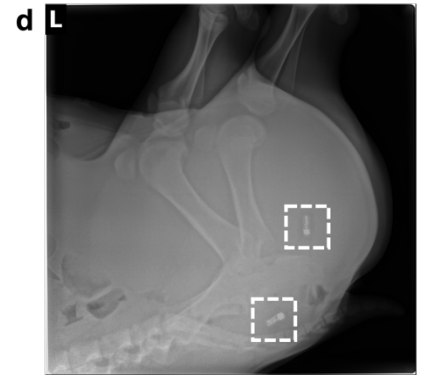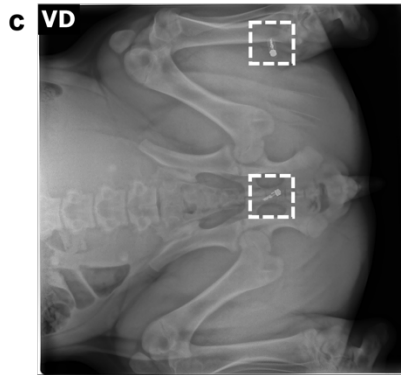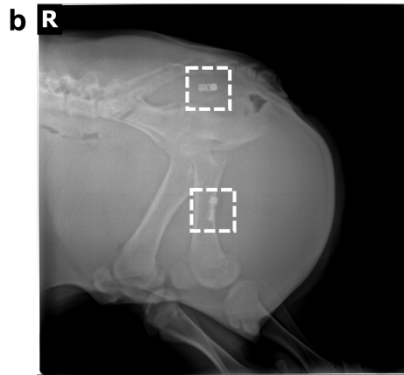
Fig. 5: (a) *In vivo* measurement data when iMAG is located inside the colon of the pig. The ground truth (21.37cm) is obtained using orthogonal X-rays taken from the **(b)** right, **(c)** vertical, and **(d)** left side of the animal. The decoded distance of iMAG from the external reference iMAG is 20.20 $\pm$ 0.01 cm (mean $\pm$ std). Individual errors in the X and Y components of the decoded distance are >5mm, which is an artifact caused by the X-ray acquisition methodology, as explained in the Methods section.

iMAG in Rectum

Ground truth from
X-rays: 20.00cm

a *In vivo* **Measurement Data**

| Trial	Decoded Distance (cm)	|X-Error| (mm)	|Y-Error| (mm)	|Z-Error| (mm)
1	19.7439	1.1730	0.3100	2.2558
2	18.9950	1.0631	3.2464	4.4520
3	19.6098	1.1993	0.3170	3.6992
Mean	19.4496 $\pm$ 0.3993	1.1451	1.2911	3.4690
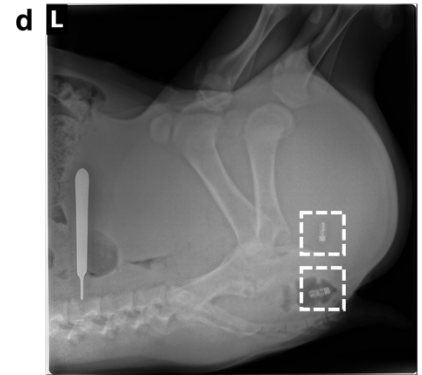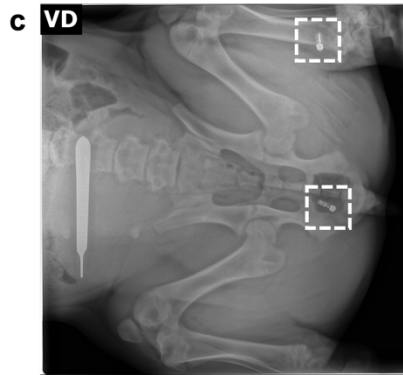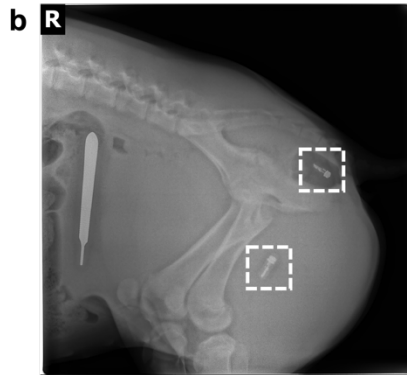
Fig. 6: (a) *In vivo* measurement data when iMAG is located inside the rectum of the pig. The ground truth (20.00cm) is obtained using orthogonal X-rays taken from the **(b)** right, **(c)** vertical, and **(d)** left side of the animal. The decoded distance of iMAG from the external reference iMAG is 19.45 $\pm$ 0.40 cm (mean $\pm$ std). Individual errors in the X, Y and Z components of the decoded distance are <5mm, the theoretical error-bound of our system.
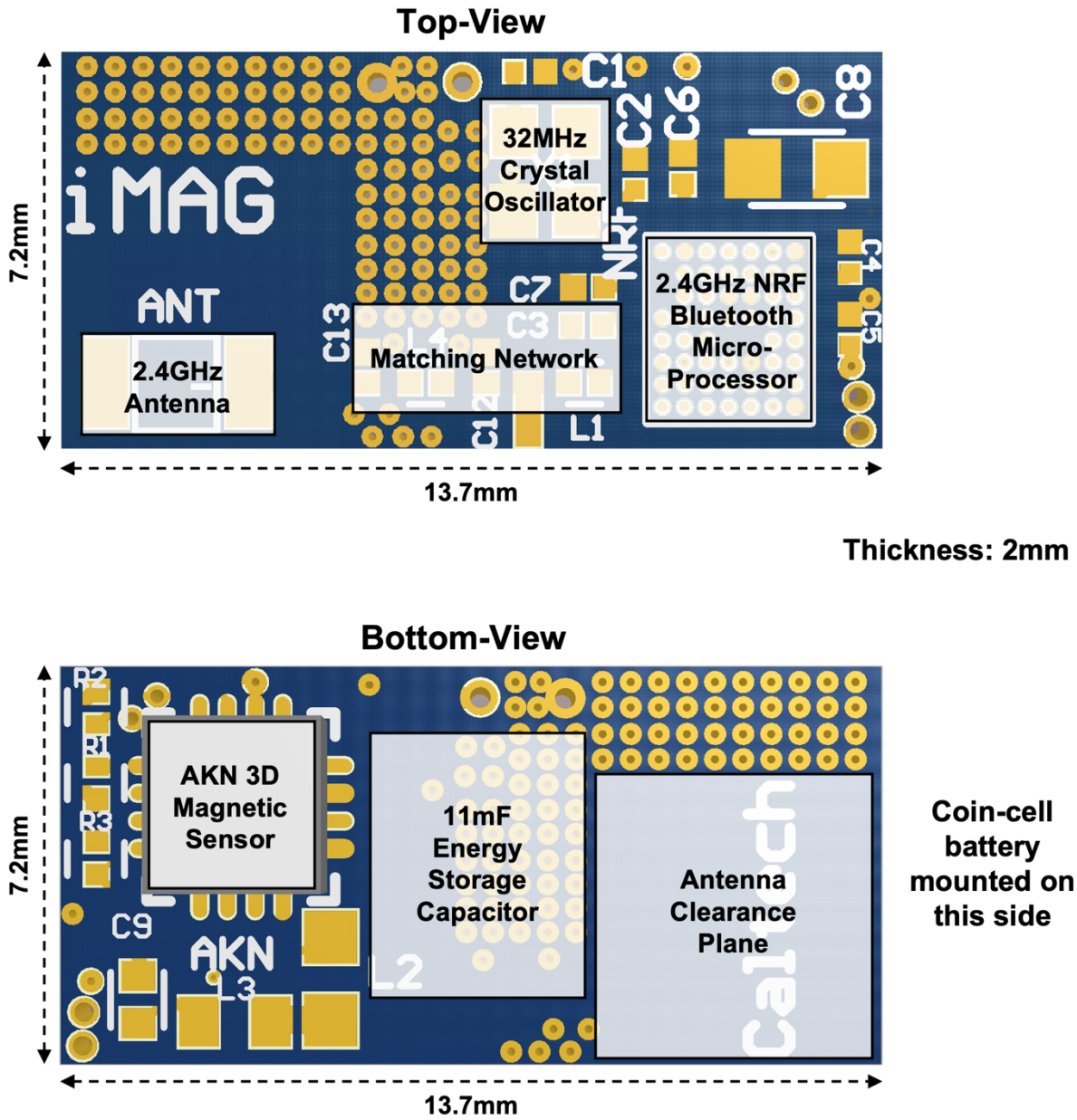
Fig. 7: Complete overview of the printed circuit board (PCB) designed for iMAG. The coin-cell battery is mounted on the side of the antenna and away from the sensor location, to avoid potential interference caused by the weakly magnetic casing of the battery.
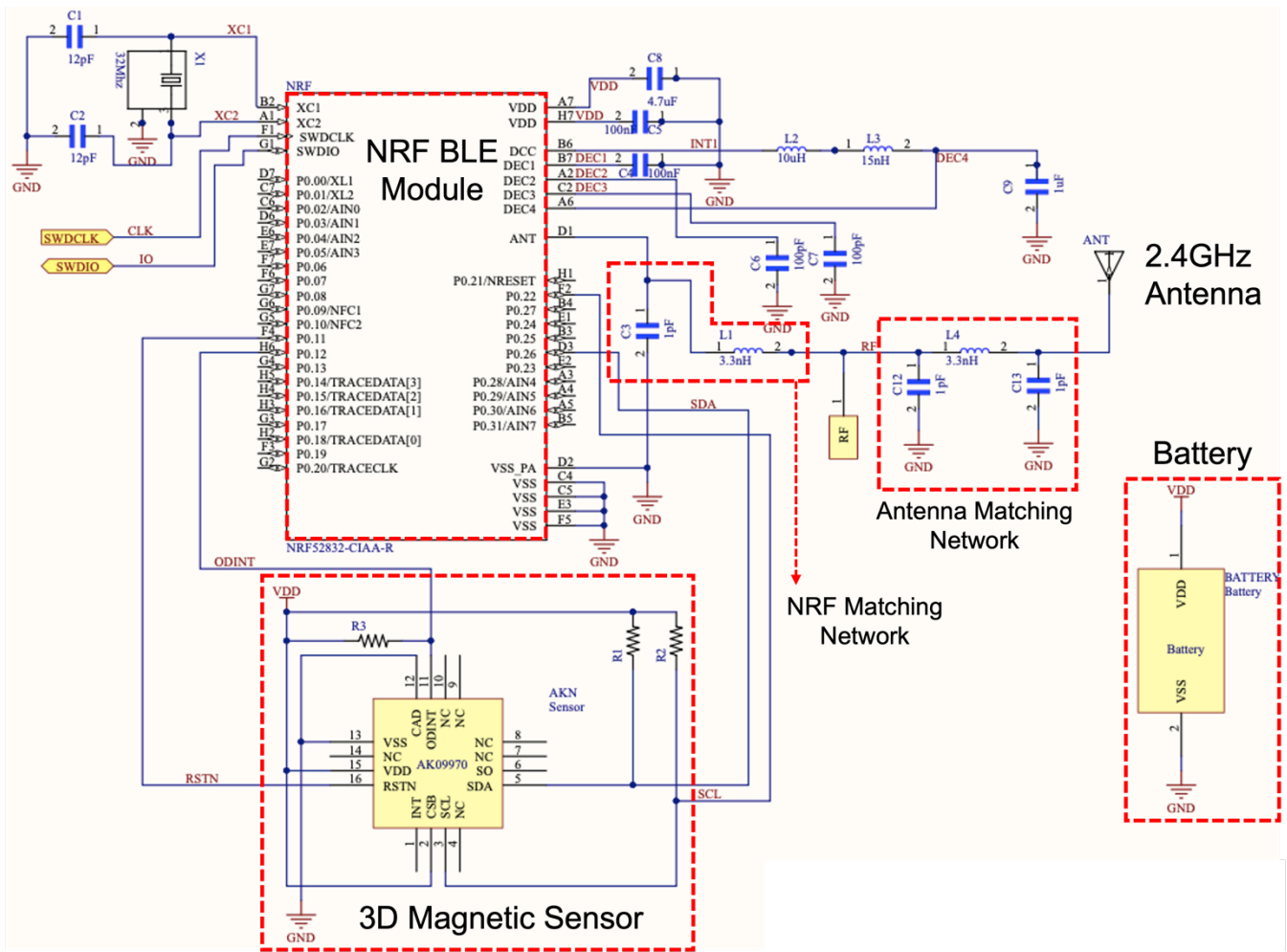
Fig. 8: Complete schematic of the iMAG device. All the circuit components and their relative interconnections are shown. The values of the components shown in both the matching networks are tuned in real time to account for the fabrication-related mismatches. The final values used in the two matching networks are shown in Fig. 2c of the main text.
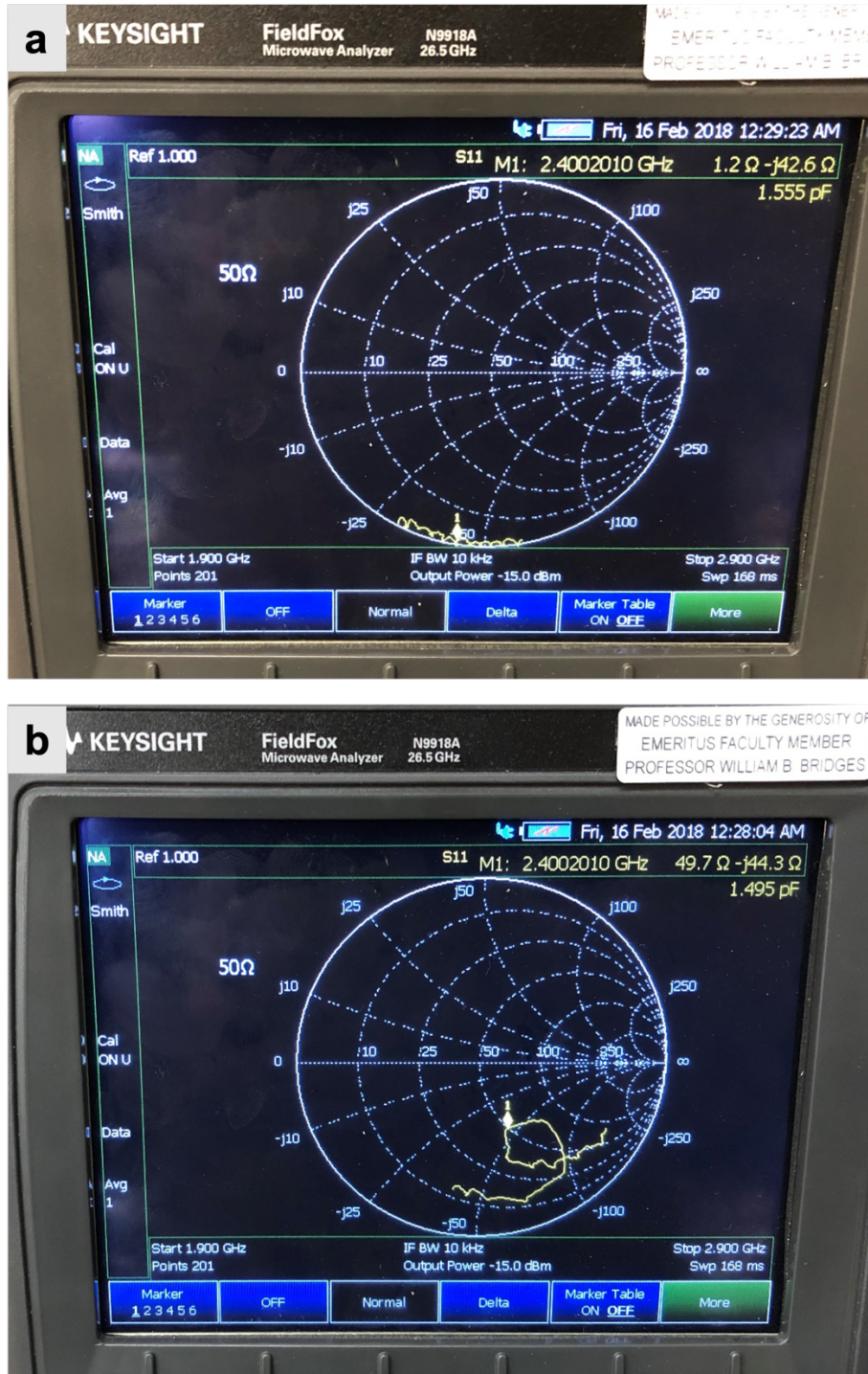
Fig. 9: Matching network tuning performed in real-time using Microwave Vector Network Analyzer (FieldFox) and Spectrum Analyzer. Impedance plot on the Smith Chart with **(a)** only the FieldFox probe (1.5pF), and **(b)** FieldFox probe connected to iMAG's RF node (50Ω + 1.5pF). The RF node is shown in Supplementary Fig. 11 (between the two matching networks). Obtaining 50Ω in (b) shows the high accuracy of the matching network used in iMAG.
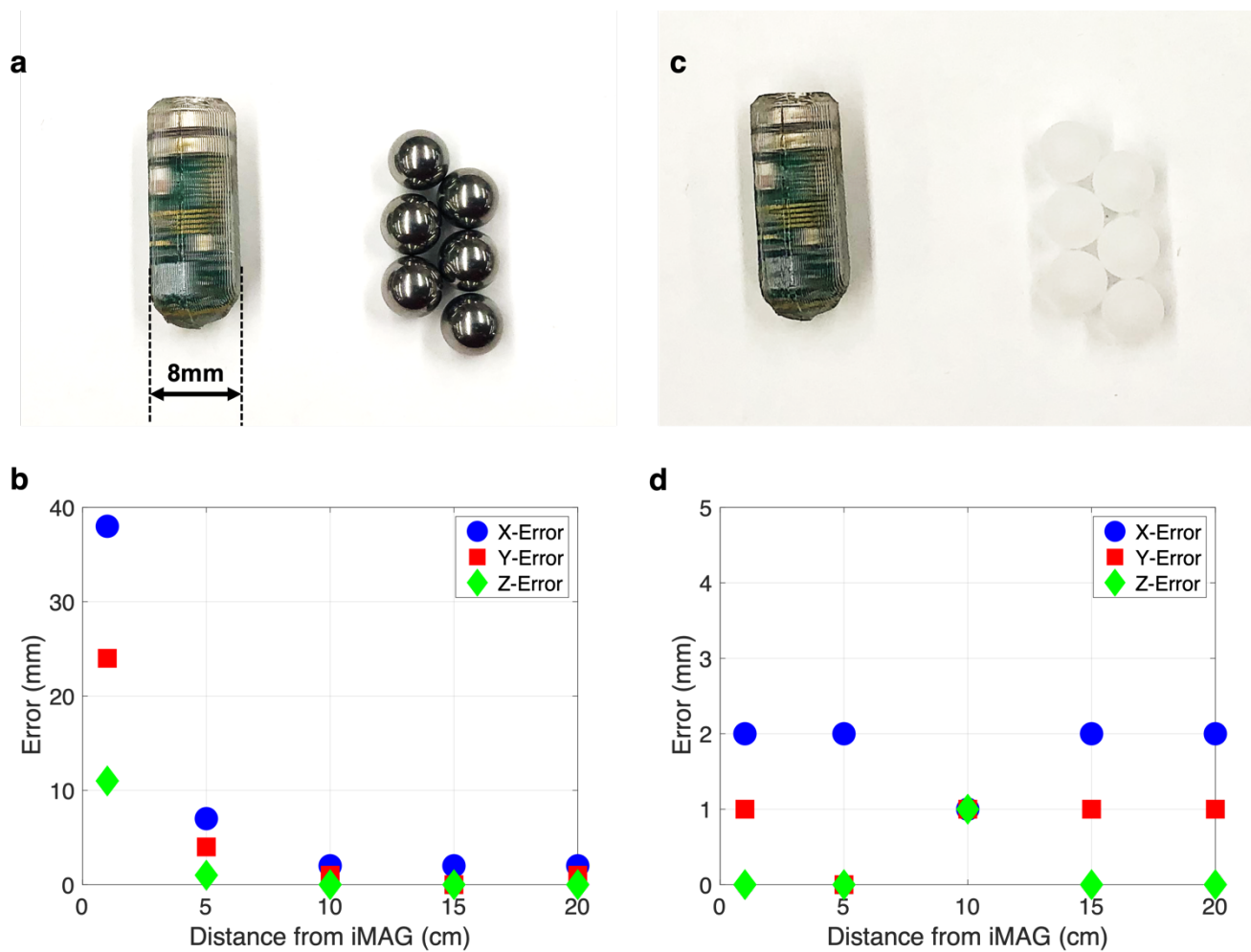
Fig. 10: Magnetic interference characterization performed by localizing an iMAG device in the presence of magnetic vs non-magnetic beads. **(a)** iMAG device shown next to highly magnetic barium beads used during the magnetic-label tracking study performed in this work (Fig. 5d-i in main manuscript). **(b)** Localization error of iMAG plotted vs distance from the barium beads. When the beads are very close to iMAG (<5cm), the error is significantly higher than the 5mm error-threshold of the system due to the distortion caused in the magnetic field by the beads. As the distance of the beads from the iMAG is increased to 10cm or higher, the error falls within the threshold limit which signifies the system's immunity to distortion caused by magnetic objects when located sufficiently away. **(c)** iMAG device shown next to non-magnetic polyethylene beads used as a negative control to compare against the interference caused by the magnetic barium beads. **(d)** Localization error of iMAG as the distance of the polyethylene beads is varied from iMAG. As seen, the error values are independent of the proximity from the beads and are within the error-threshold, highlighting the specificity of our system toward magnetic objects.
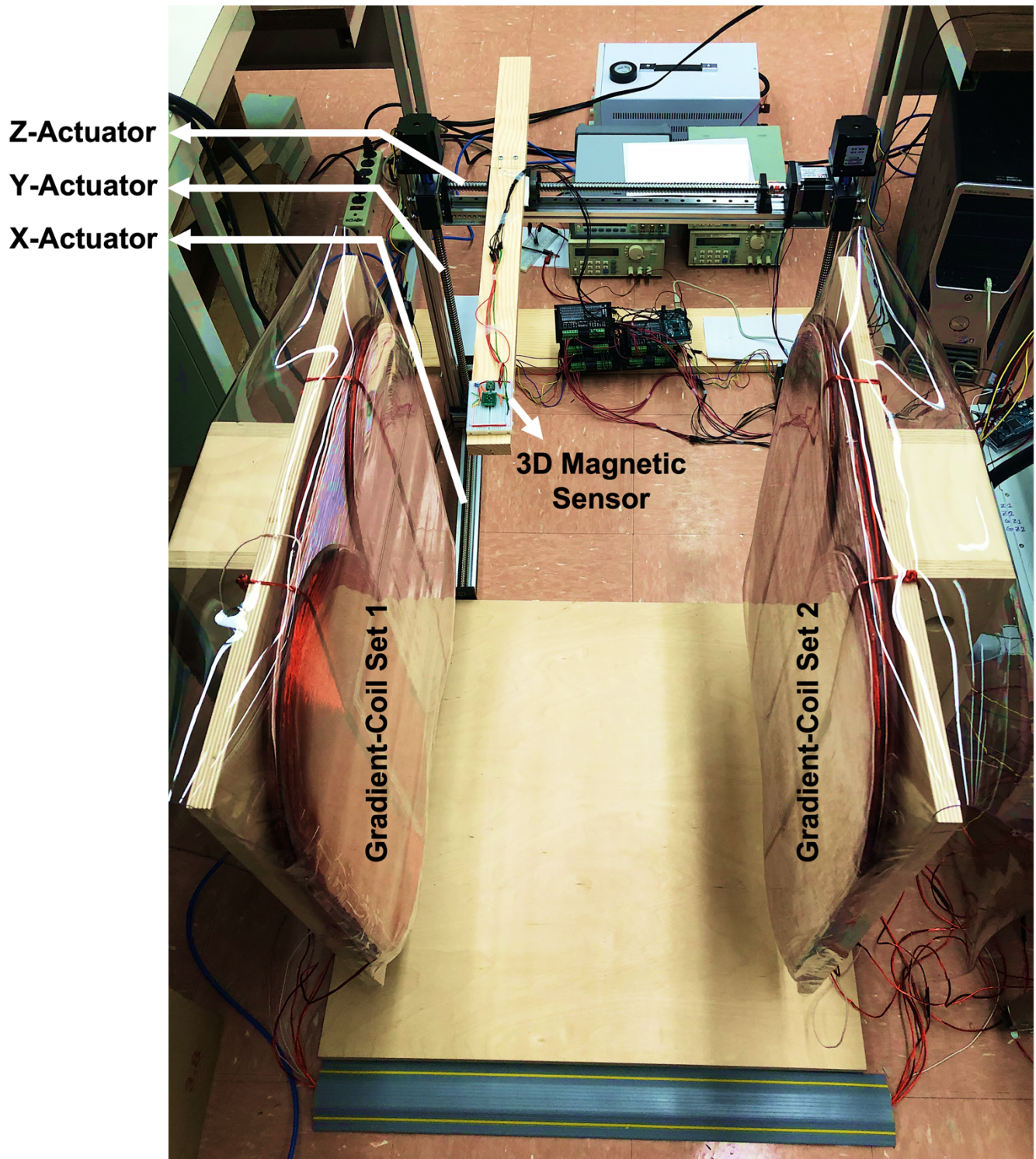
Fig. 11: Setup for characterizing the magnetic field gradients produced by the coils in the FOV. A 3D magnetic sensor mounted on a wooden arm is moved in the FOV in increments of 1cm in the X, Y and Z directions using three orthogonally connected linear actuators. The magnetic field data measured by the sensor at each step is stored, interpolated (to achieve 1mm resolution), and then used for creating an LUT for position decoding during the localization experiments. More details in [25].
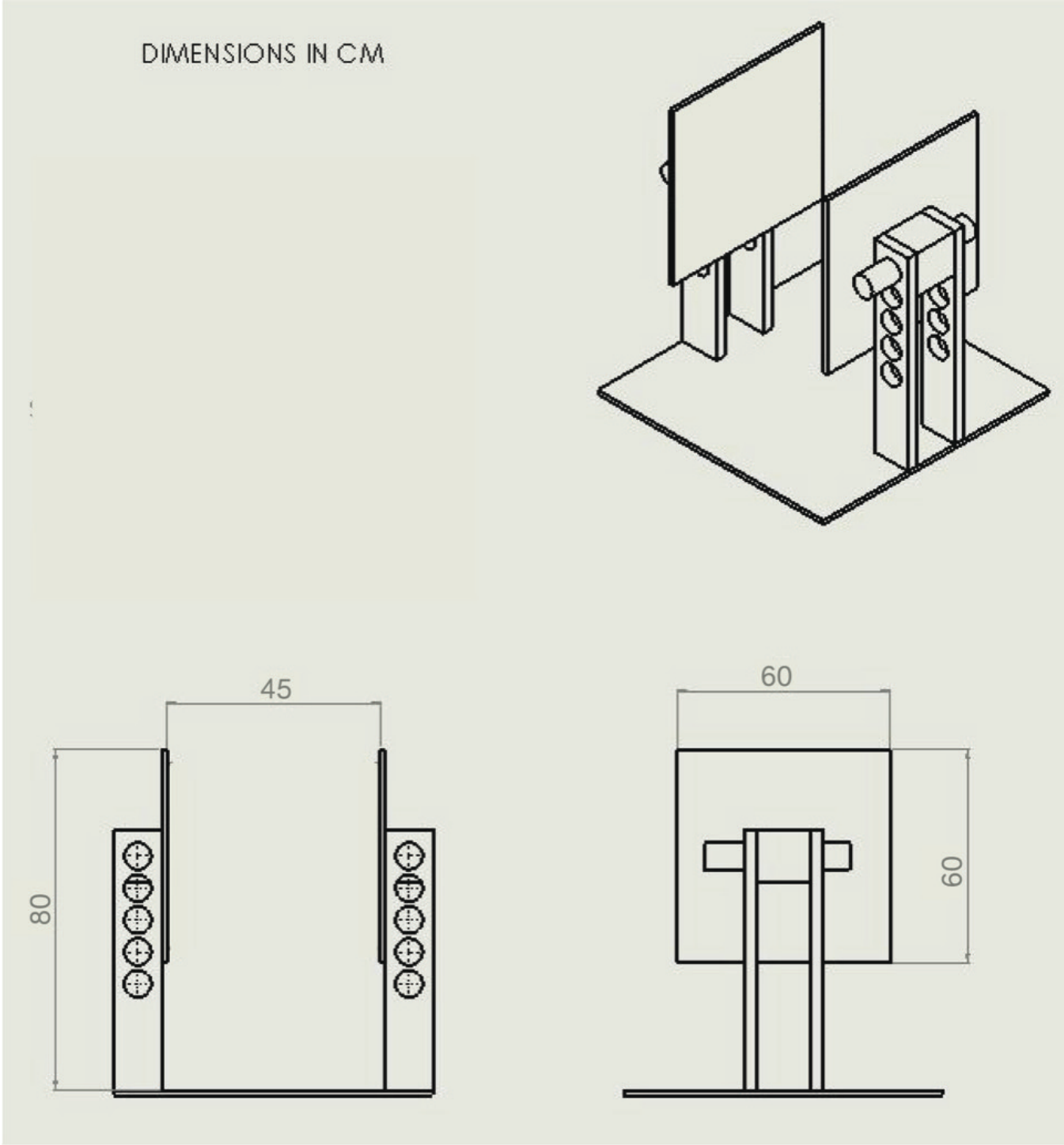
Fig. 12: Design specifications of the wooden chute with adjustable height for the coil-mounting walls.
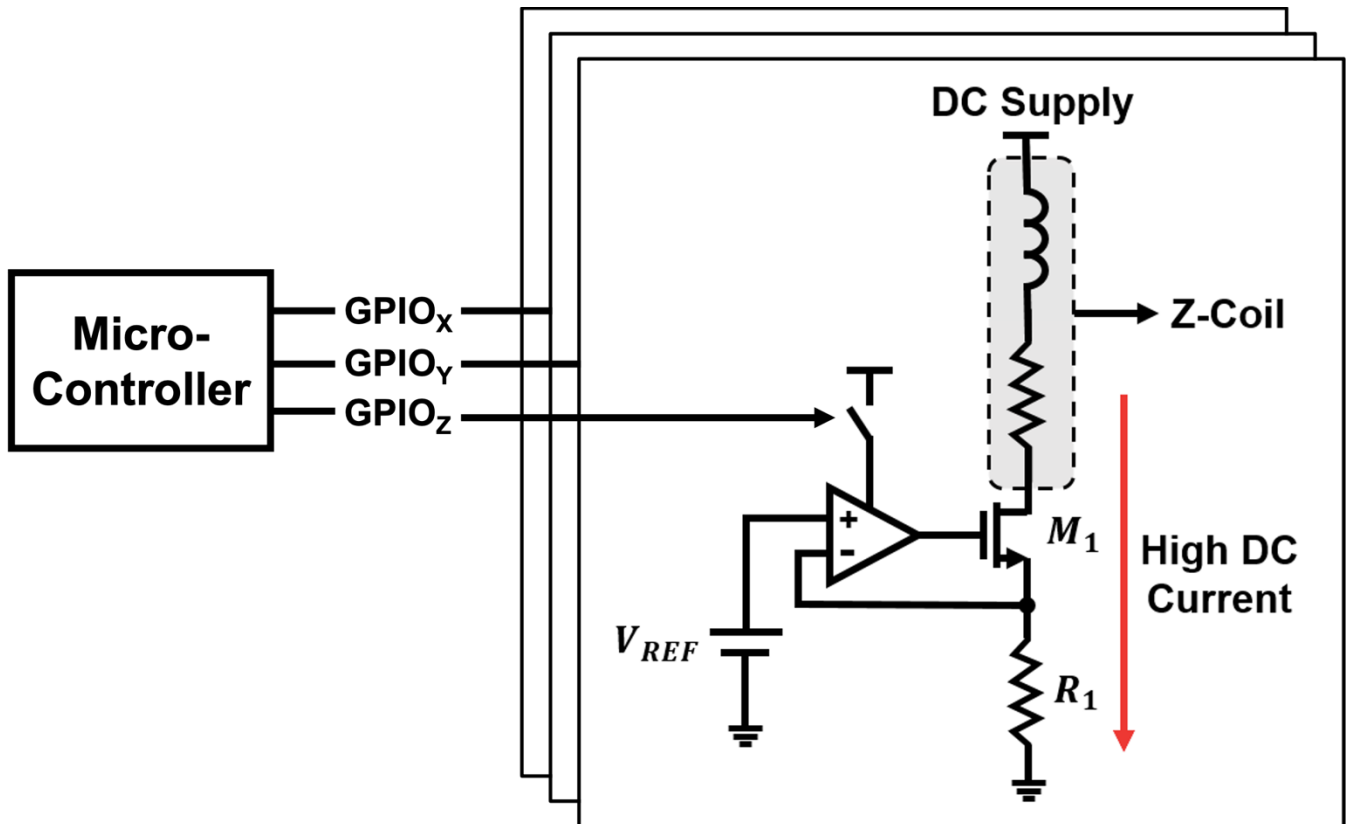
Fig. 13: Overview of the gradient coil controller circuit. V_{REF} and R_1 together set the value of the DC current since $I_{DC} = V_{REF}/R_1$. An N-channel MOSFET driver M_1 (FDL100N50F) rated for 500V and 100A is used for handling the high DC current coming into the coils. R_1 is chosen with high temperature stability (MP930-0.020-5%) to ensure a thermally stable current value. The coil control is established by the GPIO pins connected to a microcontroller (nRF52DK or Arduino) that serve as the coil enable (ENA) signals.

Main LUT	X	Y	Z	B_X	B_Y	B_Z
	x_0	y_0	z_0	B_{x0}	B_{y0}	B_{z0}
	x_1	y_1	z_1	B_{x1}	B_{y1}	B_{z1}
	x_2	y_2	z_2	B_{x2}	B_{y2}	B_{z2}
	x_3	y_3	z_3	B_{x3}	B_{y3}	B_{z3}
	x_4	y_4	z_4	B_{x4}	B_{y4}	B_{z4}
	⋮	⋮	⋮	⋮	⋮	⋮
	x_n	y_n	z_n	B_{xn}	B_{yn}	B_{zn}

LUT-X	X	Y	Z	B_X	B_Y	B_Z
	x_2	y_2	z_2	B_{x2}	B_{y2}	B_{z2}
	x_5	y_5	z_5	B_{x5}	B_{y5}	B_{z5}
	x_{21}	y_{21}	z_{21}	B_{x21}	B_{y21}	B_{z21}
	x_{78}	y_{78}	z_{78}	B_{x78}	B_{y78}	B_{z78}
	x_{567}	y_{567}	z_{567}	B_{x567}	B_{y567}	B_{z567}
	x_{1050}	y_{1050}	z_{1050}	B_{x1050}	B_{y1050}	B_{z1050}

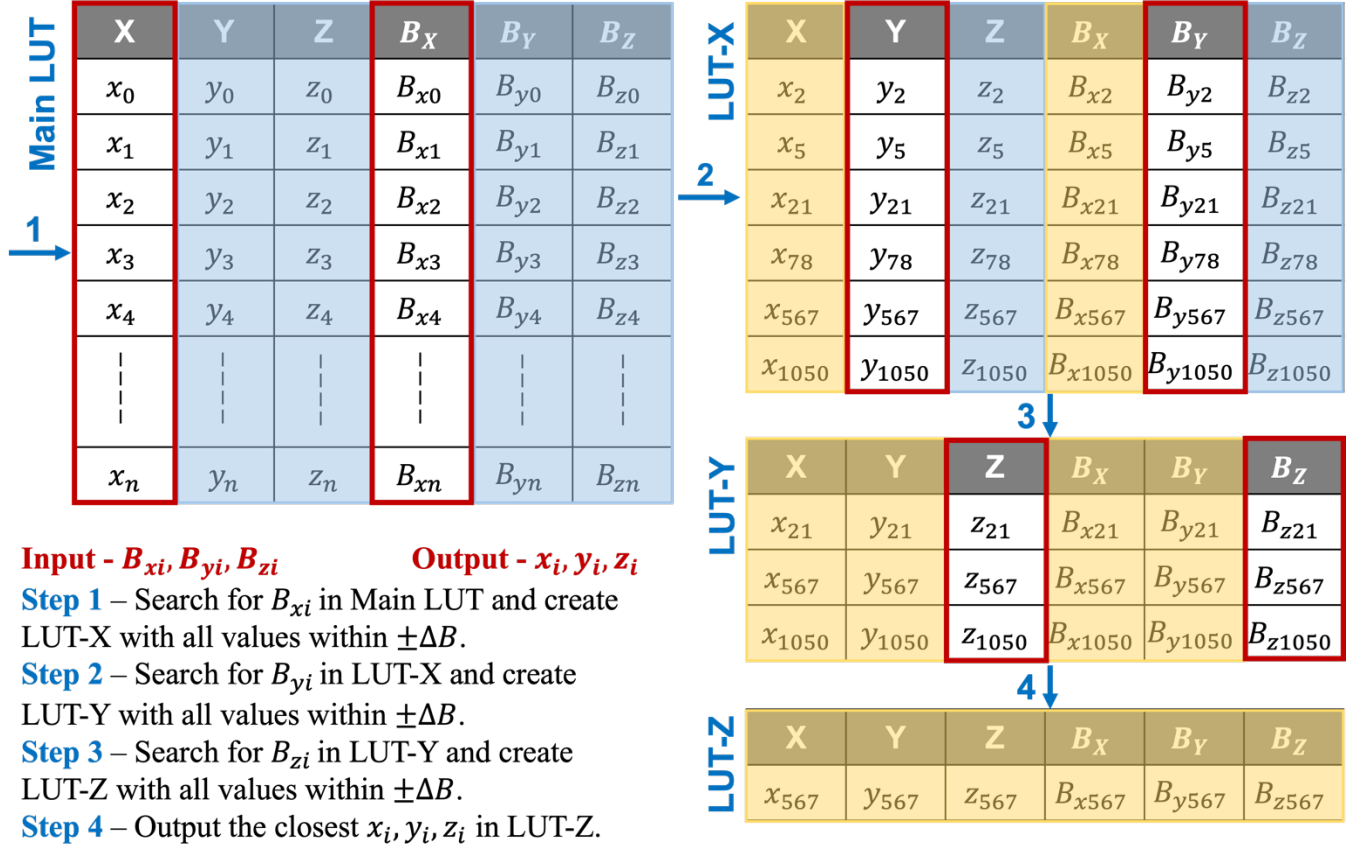| LUT-Y	X	Y	Z	B_X	B_Y	B_Z
	x_{21}	y_{21}	z_{21}	B_{x21}	B_{y21}	B_{z21}
	x_{567}	y_{567}	z_{567}	B_{x567}	B_{y567}	B_{z567}
	x_{1050}	y_{1050}	z_{1050}	B_{x1050}	B_{y1050}	B_{z1050}

LUT-Z	X	Y	Z	B_X	B_Y	B_Z
	x_{567}	y_{567}	z_{567}	B_{x567}	B_{y567}	B_{z567}

Input - B_{xi}, B_{yi}, B_{zi} **Output -** x_i, y_i, z_i

Step 1 – Search for B_{xi} in Main LUT and create LUT-X with all values within $\pm \Delta B$.

Step 2 – Search for B_{yi} in LUT-X and create LUT-Y with all values within $\pm \Delta B$.

Step 3 – Search for B_{zi} in LUT-Y and create LUT-Z with all values within $\pm \Delta B$.

Step 4 – Output the closest x_i, y_i, z_i in LUT-Z.

Fig. 14: Overview of the 3D search algorithm for position decoding from the magnetic field values measured by iMAG. More details in [25].
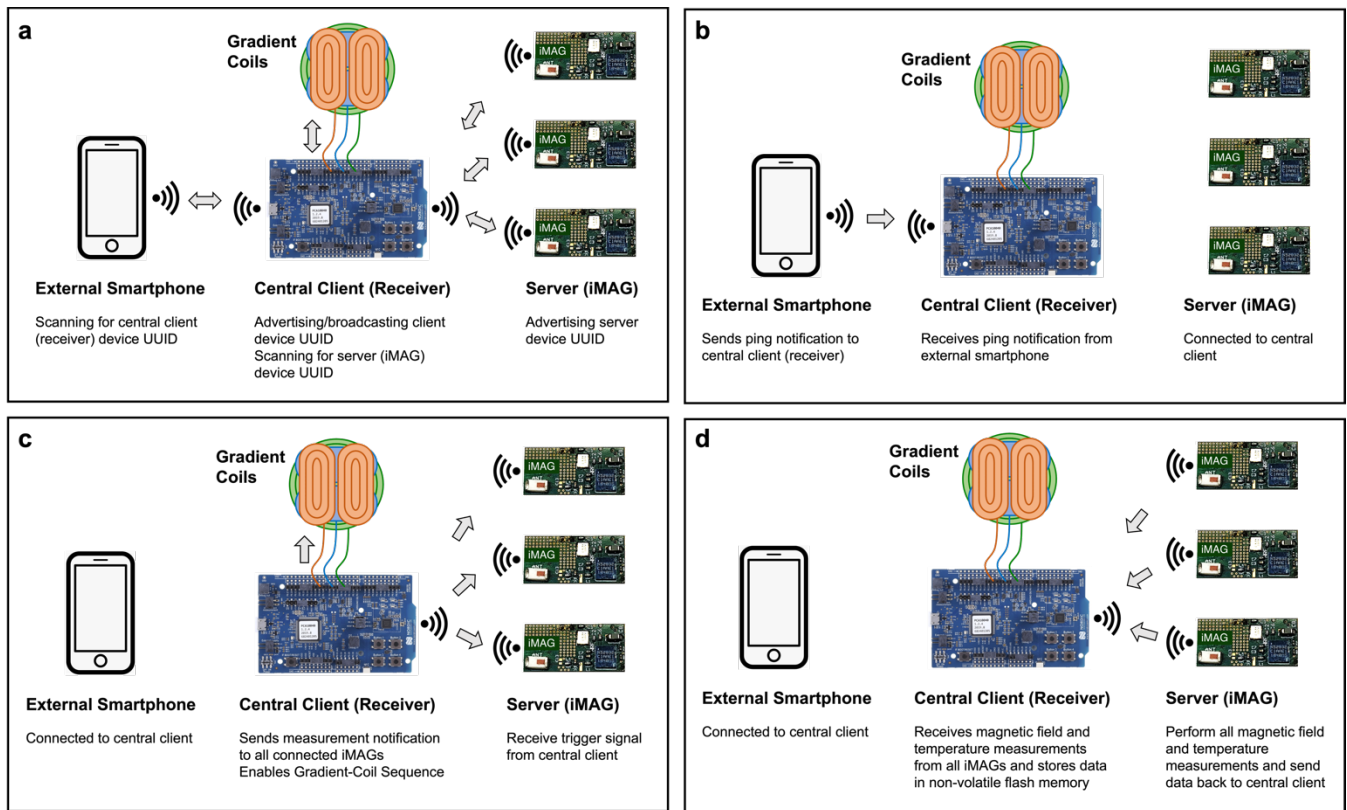
Fig. 15: (a) iMAG's system-connection procedure for all constituent components. **(b)** Measurement initiation from the external smartphone. **(c)** Central client (receiver board) receives the notification from the smartphone and triggers measurements by sending signals to all the connected servers (iMAGs) and enabling the required gradient coil sequence. **(d)** iMAGs perform all magnetic field and temperature measurements and send them to the central client, which stores all the data in flash memory and prints it out on a computer that it is connected to.

Table-I: iMAG's Power Consumption Summary

iMAG's Operation Mode	DC/DC Regulator Disabled: Current Consumption	DC/DC Regulator Enabled: Current Consumption
System Off Idle-mode	0.3µA	0.3µA
System On Idle-mode	10µA	8µA
Peak Consumption during Advertising	15mA	8mA
Average Consumption during Advertising	440µA	230µA
Connection Mode Standby	120µA	80µA
Peak Consumption during I2C Data Transmission	13mA	6mA
Average Consumption during I2C Data Transmission	250µA	180µA

To make the iMAG highly power-efficient, the DC/DC regulator for the NRF BLE chipset is enabled which results in almost 2x power saving (comparing the right two columns in the above table).

Extended Data Fig. 3 Video:
DOI on figshare (https://figshare.com/): 10.6084/m9.figshare.24076089

Extended Data Fig. 4 Video:
DOI on figshare (https://figshare.com/): 10.6084/m9.figshare.24078711